mater.scichina.com link.springer.com

# **Defect Tolerance in Chalcogenide Perovskite Photovoltaic Material BaZrS**<sub>3</sub>

Xiaowei Wu<sup>1,†</sup>, Weiwei Gao<sup>2,3,†</sup>, Jun Chai<sup>1</sup>, Chen Ming<sup>1,\*</sup>, Miaogen Chen<sup>4</sup>, Hao Zeng<sup>5</sup>, Peihong Zhang<sup>5</sup>, Shengbai Zhang<sup>6</sup> and Yi-Yang Sun<sup>1,\*</sup>

ABSTRACT Chalcogenide perovskites exhibiting lower band gaps than oxide perovskites and higher stability than halide perovskites are promising materials for photovoltaic and optoelectronic applications. For such applications, the absence of deep defect levels serving as recombination centers (dubbed defect tolerance) is a highly desirable property. Here, using density functional theory (DFT) calculations, we study the intrinsic defects in BaZrS<sub>3</sub>, a representative chalcogenide perovskite material. We compare Hubbard-U and hybrid functional methods, both of which have been widely used in addressing the band gap problem of semi-local functionals in DFT. We find that tuning the *U* value to obtain experimental bulk band gap and then using the obtained U value for defect calculations may result in over-localization of defect states. In the hybrid functional calculation, the band gap of BaZrS<sub>3</sub> can be accurately obtained. We observe formation of small S-atom clusters in both methods, which tend to self-passivate the defects from forming mid-gap levels. Even though in the hybrid functional calculations several relatively deep defects are observed, all of them exhibit too high formation energy to play a significant role if the materials are prepared under thermal equilibrium. BaZrS<sub>3</sub> is thus expected to exhibit sufficient defect tolerance promising for photovoltaic and optoelectronic applications.

**Keywords:** chalcogenide perovskite, photovoltaics, defect tolerance, BaZrS<sub>3</sub>, first-principles calculation

#### INTRODUCTION

In the past decade, perovskite materials have been successfully used as semiconductors for photovoltaic [1-8], photodetection [9-13] and light-emitting applications [14-20]. This is different from the traditional uses of perovskites mainly for dielectric applications, such as piezoelectrics and ferroelectrics [21,22]. The semiconducting perovskite materials intensively studied in recent years are dominated by halides [1-20]. The low conduction band due to strong spin-orbit coupling in cations such as lead and the high valence band due to the anions such as iodine 6p orbitals synergically reduce the band gap of the halide perovskites to a region suited for photovoltaic devices [23]. Other interesting physics such as defect tolerance allows the materials to be readily prepared for device fabrication with less needs for high purity and high crystallinity while maintaining the low production cost. Currently, two main barriers for the halide perovskites to be deployed in larger scale are the stability issue partly caused by the organic components and the toxicity mainly due to the use of lead [24,25].

Chalcogenide perovskites (CPs) was first synthesized in 1957 [26]. Since then, while a number of CPs have been reported, their physical properties have only been studied sporadically [27–29]. Inspired by the success of halide perovskites, CPs have been proposed for photovoltaic applications [30–32]. The optical properties of II-IV-S<sub>3</sub> CPs have been studied experimentally [31,33,34]. These CPs are air stable and contain only non-toxic elements. Among them, BaZrS<sub>3</sub> having a band gap of about 1.8 eV [31,33–35] is suited for making solar cells, in particular, when combined

<sup>1</sup> State Key Laboratory of High Performance Ceramics and Superfine Microstructure, Shanghai Institute of Ceramics, Chinese Academy of Sciences, Shanghai 201899, China

<sup>2</sup> School of Physics, Dalian University Technology, Dalian 116024, China

 $<sup>3\</sup> Center for Computational\ Materials, Oden\ Institute\ for\ Computational\ Engineering\ and\ Sciences,\ The\ University\ of\ Texas\ at\ Austin,\ TX\ 78712,\ United\ States$ 

<sup>4</sup> College of Science, China Jiliang University, Hangzhou 310018, China

<sup>5</sup> Department of Physics, University at Buffalo, The State University of New York, Buffalo, NY 14260, United States

<sup>6</sup> Department of Physics, Applied Physics & Astronomy, Rensselaer Polytechnic Institute, Troy, NY 12180, United States

 $<sup>\</sup>ensuremath{^{\dagger}}$  These authors contributed equally to this work.

<sup>\*</sup> Corresponding authors (emails:  $\underline{vysun@mailsic.ac.cn} \ (Sun\ YY); \\ \underline{mingchen@mailsic.ac.cn} \ (Ming\ C))$ 

with silicon-based solar cells for two-junction tandem solar cells. Ti-doping has been attempted to optimize solar light absorption by reducing the band gap [31,36]. Thin films of BaZrS $_3$  have also been prepared with their electronic and optical properties being reported [37–39]. Encouragingly, SrHfS $_3$  has been experimentally demonstrated to exhibit excellent green light emitting properties [40]. Recently, we found that III-III-S $_3$  CPs could possess wider band gaps than II-IV-S $_3$  CPs and hold promise for broader applications such as transparent conducting materials [41].

With the attractive application potentials, it is of great interest to understand the defect properties of CPs because defect tolerance has been considered as one of the unique properties of halide perovskites [42–49]. For photovoltaic and optoelectronic materials, recombination centers are the defects to be avoided as they compete with the desired functions of carriers, *i.e.*, producing current or light. It has been shown that intrinsic defects in halide perovskites are mostly shallow defects, which do not serve as effective recombination centers [42] Such a property allows low-cost synthesis of the materials and low-cost fabrication of the devices without demanding control on structural defects.

The defect properties of BaZrS<sub>3</sub> were studied by density functional theory (DFT), where Hubbard U of 4.5 eV was applied to Zr 4d orbitals to obtain the experimental band gap [31]. Usually, 4d transition metals (TMs) have much delocalized d orbitals than 3 d TMs. While using *U* values of about 4.5 eV may be appropriate for the 3 d TMs, they are too large for 4 d TMs. Large U values could result in over-localized d orbitals and in turn affect the defect properties. Regarding the band gap problem in DFT, the hybrid functional of Heyd, Scuseria and Ernzerhof (HSE) by partly incorporating Hartree-Fock exchange is particularly useful for the CPs. The predicted band gaps using the HSE functional are in good agreement with experiments without tuning the empirical parameters of HSE. It is therefore desirable to study the defect properties using the HSE functional

In this paper, we report a comparative study on the defect properties of BaZrS3 using different functionals. We start from the semi-local PBEsol functional. Then, by systematically tuning the *U* value for Zr 4d we illustrate the effect of Hubbard *U* on the defect properties. It is found that the defect level could undergo a sudden transition from shallow to deep when *U* is above a threshold. We then carry out first-principles calculation on the U value of Zr 4d in BaZrS3 and show that the *U* value is as small as 1.1 eV and produces shallow defect levels only. Finally, to achieve more conclusive results on the defect properties of BaZrS3, we calculate the defect transition levels and defect formation energies using the HSE functional. While several defects with relatively deep levels have been identified, their high formation energy suggests that they can be avoided under thermal equilibrium. Together, these results show that BaZrS<sub>3</sub> is substantially defect tolerant for photovoltaic and optoelectronic applications.

#### COMPUTATIANAL METHODS

DFT calculations were carried out using Vienna ab initio simulation (VASP) package [50,51], which describes the interaction between the ion-cores and valence electrons by projector augmented wave (PAW) potentials [52]. Plane waves with cutoff energy of 20 Ry were taken as basis set. Different exchange-correlation functionals were adopted, namely, PBEsol [53], PBEsol+U [54] and HSE [55]. The supercell method was used to model the defects. A 160-atom supercell was constructed from the 20-atom unit cell by a conversion matrix of (2 0 0: 0 1 -1: 0 2 2). The  $\Gamma$ point was used to represent the Brillouin zone. Calculations were spin-polarized if a defect possesses a magnetic moment. The atomic structures were fully relaxed until the calculated forces on all atoms were less than 1 mRy/Both. The lattice constants were optimized by using each functional with increased cutoff energy of 30 Ry and compared with experimental results in Table I. A 3×2×3 Monkhorst-Pack k-point grid was used in the bulk calculations.

**Table 1** Lattice constants of BaZrS $_3$  optimized by different functionals and used in defect calculations. In the PBEsol+U calculation, the U value is determined from first-principles calculation as described in the text. Experimental results [56] are also listed for comparison.

Functional	a (Å)	b (Å)	c (Å)
PBEsol	7.118	9.932	6.953
PBEsol+U	7.121	9.961	6.976
HSE	7.148	10.020	7.024
Experimental	7.060	9.981	7.025

The formation energy of a point defect carrying a charge q was calculated following [57,58]

(1)

is the is the total energy of the supercell where containing a point defect of charge q,  $E_0$  is the total energy of the perfect supercell,  $n_i$  is the number of atoms which are added  $(n_i < 0)$  or removed  $(n_i > 0)$  from the supercell during the formation of the defects,  $\mu_i$  is the chemical potential of the constituent element i referenced to the total energy per atom of element i in its stable phase  $(E_i)$ ,  $E_F$  is the Fermi energy referenced to the valence band maximum (VBM) of the host material ( $E_{VBM}$ ). The allowed range for  $\mu_i$  is determined by the existence of various secondary phases, which will be described in more details below. The Fermi energy  $E_{\rm F}$ generally varies between  $E_{VBM}$  and the conduction band minimum (CBM) of the host material. The defect transition level, at which the thermodynamically stable charge state of the defect switches from q to q', is given

by

which indicates whether the defect is deep or shallow.

First-principles calculation on the Hubbard U and I parameters were conducted with the constrained random phase approximation (cRPA)[59]. The details of our code implementation are presented in Refs. [60,61]. Here we briefly review the main steps. We first perform DFT calculations with planewave-based pseudopotential code PARATEC[62] to prepare a set of frontier Kohn-Sham states and projections of Zr d orbitals on these states. Using Zr d orbitals as the initial guesses, we construct maximally localized Wannier functions using Wannier90 code[63]. Next, we use BerkeleyGW code[64] to calculate cRPA screened Coulomb potential Then, the interaction matrix elements  $\langle ij | W^{\text{RPA}} | ij \rangle$  and  $\langle ij | W^{\text{RPA}} | ji \rangle$  are computed, where i, jare Wannier function indices. Finally, the Hubbard Uand J parameters are obtained by U = 1/25 $\sum_{ij} \langle ij | W^{\text{RPA}} | ij \rangle$  and  $J = 1/20 \sum_{i \neq j} \langle ij | W^{\text{RPA}} | ji \rangle$ , respective-

#### RESULTS AND DISCUSSION

Recombination centers and carrier traps. Before describing the results, we first explain the recombination centers (RCs) to be studied in this work. Figure 1 shows the two types of RCs through a Shockley-Read-Hall (SRH) process. The type I RC starts from a neutral defect. In step 1, it captures an electron and becomes a negative center. In step 2, the negative center will scatter electrons, but capture a hole. In step 3, the captured electron and hole recombine and accomplish a SRH process. The type I RC could also capture a hole first in step 1, and then capture an electron in step 2.

The type II RC starts from a charged defect. While Figure 1 shows the negatively charged case, starting from a positively charged defect can be treated similarly. For type II RC, in step 2, the negative center captures a hole first and in step 3 it captures an electron. Then, the step 3 will be the same as that in type I RC. Even though in step 2, the neutral center has a similar chance of capturing a hole, this process cannot accomplish a SRH process. Therefore, as long as one hole is re-emitted, it will be able to capture an electron.

It is necessary to differentiate the RCs from carrier traps. Figure 1 illustrates the case for a defect carrying 2— charge. The discussion below applies to charges higher than 1 regardless of the charge types. In the case of 2— charge, the defect will capture a hole in step 1. Then, in step 2, because it is still a negative center, it cannot capture an electron to accomplish a SRH process. Instead, it will capture another hole. Thus, in step 3 no recombination could occur.

Based on the discussions above, we know that only the  $\varepsilon(0/-)$  and  $\varepsilon(+/0)$  levels are responsible for the

SRH recombination. For this reason, we will only discuss the  $\varepsilon(0/-)$  and  $\varepsilon(+/0)$  levels below. This provides another advantage: for singly charged defects, the error due to image charge interaction under periodic boundary condition can be neglected. For our case, with a supercell size of about 15.9 Å and calculated relative dielectric constant of 12, we estimate the error to be smaller than 0.1 eV using the Madelung correction [65].

	initial	Step 1	Step 2	Step 3
RC type I	0	e	6. 5. 0. 1. 1. 1. 1. 1. 1. 1. 1. 1. 1. 1. 1. 1.	recombination
RC type II	Θ	# W W W W W W W W W W W W W W W W W W W	e- • ~~ h-*	recombination
Trap	⊛	6 h	To San Ario	NO recombination

Figure 1 Schematic showing the difference between recombination centers (RCs) and carrier traps.

Effect of Hubbard U on defect properties. We considered 12 possible intrinsic point defects, namely, vacancies ( $V_{Ba}$ ,  $V_{Zr}$ ,  $V_{S}$ ), interstitials ( $Ba_{i}$ ,  $Zr_{i}$ ,  $S_{i}$ ) and anti-site substitutions ( $Ba_{Zr}$ ,  $Zr_{Ba}$ ,  $Ba_{S}$ ,  $S_{Ba}$ ,  $Zr_{S}$ ,  $S_{Zr}$ ). We first show the results from semi-local PBEsol functional. Figure 2a shows the calculated transition levels. It is seen that all defects have transition levels around band edges or outside the band gap.  $V_{Ba}$  and  $Ba_{Zr}$  are shallow acceptors, while  $V_{S}$ ,  $Ba_{i}$ ,  $Zr_{i}$ ,  $Zr_{Ba}$ ,  $Ba_{S}$  and  $Zr_{S}$  are shallow donors.  $V_{Zr}$ ,  $S_{i}$ ,  $S_{Ba}$  and  $S_{Zr}$  behave as fully self-passivated defects with their donor levels near the VBM and acceptor levels above the CBM. We will further discuss the defect behaviors in detail below.

The issue with the PBEsol functional is the well-known band-gap problem, which results in a severely underestimated band gap of 0.86 eV. The Hubbard U (i.e., the on-site Coulomb interaction) could partly compensate for the self-interaction error of the semi-local functionals and correct the over-delocalization of the local orbitals. A side effect of the Hubbard U is the opening up of the band gap of semiconductors. This has been widely used to address the band gap problem of DFT in defect studies.

Meng et al. [31] investigated the defect transition levels of  $BaZrS_3$  using PBE+U method. The value of U was set to be 4.5 eV, which yielded a band gap of 1.72 eV, consistent with experimental results. In this study, several defects have been reported to be deep-level de-

fects, including  $S_i$ ,  $S_{Zr}$ ,  $S_{Ba}$ ,  $Zr_i$  and  $Zr_S$ . In particular,  $S_{Zr}$  exhibits a deep  $\varepsilon(0/-)$  transition level at about 0.4 eV above the VBM. This result contradicts the PBEsol results as shown in Figure 2a. Take this defect as an example, we carried out a U-dependent defect study to understand the reason for the deep transition level found in the PBE+U calculation.

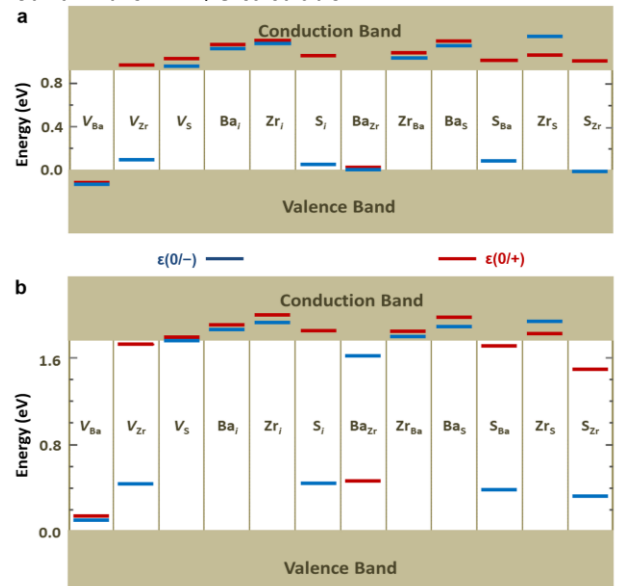


Figure 2 Defect transition levels in  $BaZrS_3$  calculated by (a) PBEsol and (b) HSE functionals.

Figure 3a shows the variations of the band gap and the  $\varepsilon(0/-)$  level of  $S_{Zr}$  as a function of U. For each Uvalue from 0 to 4.5 eV, we re-optimized the defect structures at both the neutral and 1- charge states. Totally 11 *U* values were considered. It can be seen that the band gap linearly increases with the increase of *U*. Interestingly, the  $\varepsilon(0/-)$  level undergoes a sharp transition from being inside the conduction band to being in the middle of the band gap. The transition occurs at a U value between 2.6 and 2.7 eV. Figure 3b shows a schematic of the Kohn-Sham levels at U = 2.6 and 2.7 eV near the band edges. When U = 2.6 eV, there is an electron occupying the CBM and the defect is fully delocalized as shown in Figure 3c. As a result, no local spin magnetic moment is associated with the defect. In contrast, when U = 2.7 eV, a mid-gap state appears, which is spin-polarized with the electron occupying the spin-up orbital. The corresponding mid-gap state is shown in Figure 3d, which is localized around the defect. Clearly, the localization of electronic state induced by large U value results in the deep  $\varepsilon(0/-)$  transition level.

**Determination of U value in BaZrS3.** In order to determine the U value of Zr 4d orbitals in BaZrS3, we carried out cRPA calculations based on the method described in the Method section. BaZrS3 has a 20-atom unit cell containing 4 Zr atoms and 12 S atoms with totally 20

Zr 4d orbitals and 36 S 3p orbitals, which dominate the band edge states [33]. Therefore, we constructed 56 Wannier functions using 76 Kohn-Sham orbitals covering the energy window from -5 eV to 5 eV. For the construction of Wannier functions and cRPA calculations, we used a  $4\times3\times4$  Monkhorst-Pack k-grid, a 80 Ry cutoff for wave functions, and a 30 Ry cutoff for dielectric matrix.

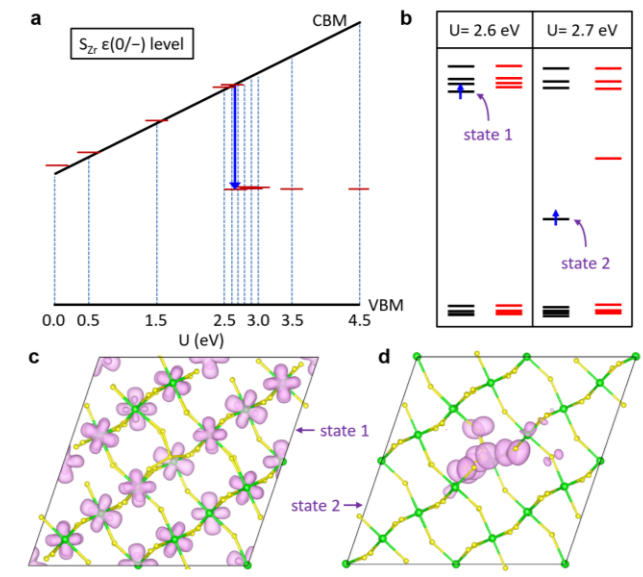


Figure 3 (a) Transition level  $\varepsilon(0/-)$  of  $S_{Zr}$  as a function of U value for Zr 4d orbital. (b) Schematic of eigenvalues near the band edges at  $\Gamma$  point of the supercell containing the  $S_{Zr}$  defect in 1- charge state calculated using U=2.6 and 2.7 eV. (c) and (d) show the charge density plots of the states 1 and 2 marked in (b).

In Figure 4a, we can see that the constructed Wannier functions display Zr 4d features. Two of them resemble  $e_{\rm g}$  orbitals and the other three resemble  $t_{\rm 2g}$ orbitals. The comparison in Figure 4b shows that the band structure interpolated with our Wannier functions well matches the band structure calculated directly with DFT. Our calculated *U* and *J* matrix elements are shown in Figure 4c. The average of the *U* matrix elements is 1.37 eV and the average of the / matrix elements is 0.24 eV. These values are significantly smaller than those of 3d or 4d late transition metal elements since Zr 4d orbitals are more spatially extended. In Figure 4d, we compare the radial parts of atomic wave functions of Zr 4d orbitals with those of Cu 3d, Ag 4d, and S 3p orbitals. Clearly, the radial atomic wave functions of Zr 4d electrons are more extended than those of Cu 3d and Ag 4d electrons, but similar to those of S 3p electrons. This comparison suggests that Zr 4d should have a smaller *U* value than those of the *d* electrons of late transition metal elements. In an alternative approach, we also calculated matrix elements  $U_{ij}' =$  $\langle d_i d_i | W^{CRPA} | d_j d_j \rangle$  and  $J_{ij}' = \langle d_i d_j | W^{CRPA} | d_i d_j \rangle$ , where the Wannier functions are replaced with  $d_i$  and  $d_j$ , the pseudo-atomic wave functions of Zr 4d orbitals. We find

 $U'=1.4~{\rm eV}$  and  $J'=0.3~{\rm eV}$ , which are close to what we find using Wannier functions and further validate our results above.

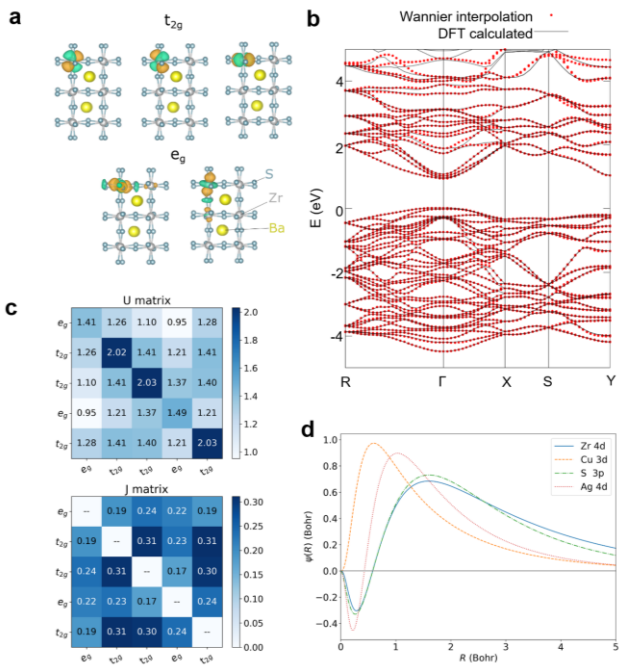


Figure 4 (a) Isosurfaces of maximally localized Wannier functions, which resemble  $\operatorname{Zr} 4ds\ t_{2g}$  and  $e_{g}$  orbitals under an octahedral crystal field (b) Comparison between the band structure calculated with DFT and that interpolated with Wannier functions. (c) Calculated elements of U and J matrices using the cRPA method. (d) Radial part of atomic wave functions of different elements calculated.

With the  $U=1.37~{\rm eV}$  and  $J=0.24~{\rm eV}$  as determined above, we recalculated the defect transition levels based on the PBEsol functional. Comparing with the results in Figure 2a, the PBEsol+U calculations yield qualitatively the same results as those from the PBEsol calculations even though the band gap is increased from 0.86 to 1.00 eV. All defects show shallow transition levels to within 0.1 eV from the band edges (see Figure S1 in Supporting Information).

**Effect of Hartree-Fock exchange.** The band gap from the PBEsol+U calculation is still about 0.8 eV smaller than experimental results. The HSE functional is known to accurately predict the band gaps for CPs [66]. We calculated the defect transition levels using the HSE functional. For easy comparison with the PBEsol results, we show the results Figure 2b. The behaviors of these defects are discussed below.

Among the three vacancy defects,  $V_{Ba}$  and  $V_{S}$  are a shallow acceptor and a shallow donor, respectively. Generally, a cation vacancy forms an acceptor, while an anion vacancy forms a donor. The Ba and S vacancies follow this rule.  $V_{Zr}$  is more complicated than the other two vacancies. It is expected to be an acceptor defect

similar to  $V_{\rm Ba}$ . However, around the Zr vacancy there are six S atoms which exhibit "dangling" bonds if viewed from a covalent-bonding picture. Our calculations show that one of the S atoms deviates from its original position and moves towards two opposite S atoms and form a S-S-S bridged trimer structure, as illustrated in Figure 5a. As a result, the  $V_{\rm Zr}$  defect unexpectedly behaves as a deep donor with the  $\varepsilon(0/+)$  transition level located at about 1.35 eV below the CBM. The structure without forming the S trimer is metastable and it is higher in energy than the S-trimer structure by 3.36 eV in the neutral state. This structure is an acceptor, as expected, with the  $\varepsilon(0/-)$  transition level 0.17 eV above the VBM.

Among the three interstitial defects, Ba<sub>1</sub> and Zr<sub>1</sub>are shallow donors. S<sub>1</sub> is expected to be an acceptor. However, a S-dimer forms as shown in Figure 5b. As a result, S<sub>1</sub> behaves as a deep donor with the  $\varepsilon(0/+)$  transition level located at about 1.33 eV below the CBM. The S-dimer serves as a 2- anion, *i.e.*,  $(S_2)^{2-}$ , similar to the S<sup>2-</sup> anion. Such kind of anion dimers are also referred to as split-interstitial defects. In some bulk sulfides, *e.g.*, pyrite FeS<sub>2</sub>, the  $(S_2)^{2-}$  anions can also be found.

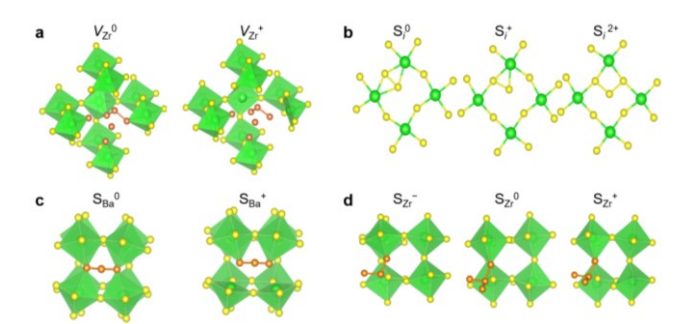


Figure 5 Atomic structures of four deep donor defects (a)  $V_{Zr}$ , (b)  $S_{li}$ , (c)  $S_{Ba}$ , and (d)  $S_{Zr}$  at different charge states. In (a), (c) and (d), the S trimer and tetramers are highlighted by a dark color.

Among the six anti-site defects,  $Ba_{Zr}$ ,  $S_{Ba}$  and  $S_{Zr}$  are expected to be acceptors, while  $Zr_{Ba}$ ,  $Ba_{S}$  and  $Zr_{S}$  are expected to be donors. However, the behavior of the  $S_{Ba}$  and  $S_{Zr}$  defects are not as expected. They behave as donors instead. Again, it is because of the formation of extra S-S bonds. In the case of  $S_{Ba}$ , a S-S-S bridge structure forms (see Figure 5c) similar to the case of  $V_{Zr}$ , while in the case of  $S_{Zr}$  a S-tetramer forms (see Figure 5d).

Overall, among all the intrinsic defects  $V_{Ba}$  is the only relatively shallow acceptor with  $\varepsilon(0/-)$  0.14 eV above the VBM, while  $V_S$ , Ba $_i$ , Zr $_i$ , Zr $_{Ba}$ , Ba $_S$  and Zr $_S$  are all shallow donors. We also checked higher charge states of these shallow defects (see Figure S2 in Supporting Information) and confirmed their shallow nature, namely, the transition levels for the higher charge states are also at the VBM (for  $V_{Ba}$ ) or CBM (for the shallow donors). We will not discuss the atomic and electronic structures of these shallow donor defects in detail below.

Among the four deep donor defects, namely,  $V_{cr}$ ,  $S_i$ , S<sub>Ba</sub> and S<sub>Zr</sub>, the formation of the S clusters (dimer, trimer and tetramer) tends to remove mid-gap states in the neutral charge state and leaves behind a relatively clean band gap. The  $\Gamma$ -point eigenvalue spectra of the four defects in the neutral charge state is shown in Figure 6, where it can be seen that the  $S_i$  and  $S_{Zr}$  defects show no gap defect states in the band gap. The removal of deep "dangling bond" states by self-passivation is desired for a semiconductor being defect tolerant. For this type of defects, usually the acceptor levels are as deep as close to the CBM and the donor levels are as deep as close to the VBM if the atomic structures of the charged states do not deviate from the neutral ones significantly. Unfortunately, structural relaxation in the 1+ state of  $V_{Zr}$ ,  $S_i$ ,  $S_{Ba}$  and  $S_{Zr}$  leads to the deep donor levels seen in Figure 2b.

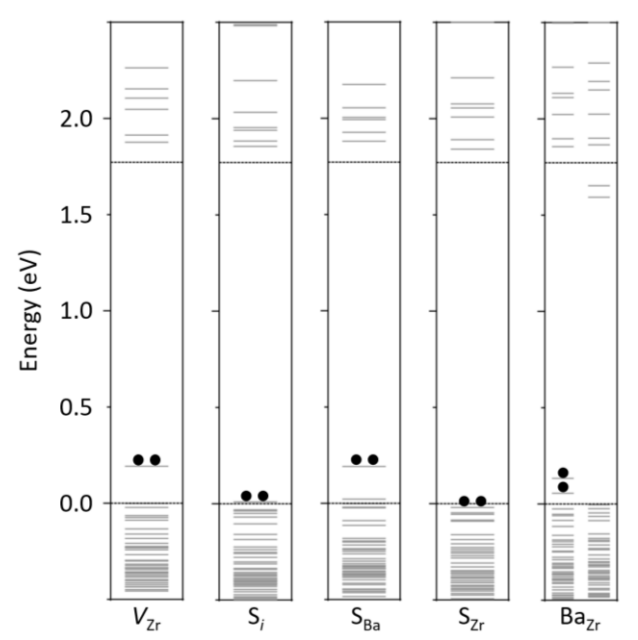


Figure 6 Eigenvalue spectra of five defects at  $\Gamma$  point of the supercell All defects are in neutral charge state. The dashed lines mark the band gap. The energy zero is aligned to the bulk VBM. The highest occupied states are marked by two dots for the four non-spin-polarized defects. For Ba<sub>Zr</sub>, which is spin-polarized, the two spin-up gap states are marked by a single dot.

Taking the  $S_I$  defect as an example, in the 1+ state it undergoes a structural change, as shown in Figure 5b, where it can be seen that one of the S-Zr bonds is broken. If further charging the defect to 2+, another S-Zr bond will be broken and the defect structure looks more like a typical interstitial defect, also shown in Figure 5b. For the other three defects, similar S-Zr bond breaking (or weakening) in the 1+ charge state results in the deep donor levels shown in Figure 5. Moreover, the  $S_{Zr}$  defect in the 1- charge state also undergoes a structural relaxation which stabilizes this charge state so that the  $S_{Zr}$  defect could also be a deep acceptor, as

shown in Figure 5d. However, the  $\varepsilon(0/-)$  transition level is much closer to the CBM compared with the PBE+U calculation using U=4.5 eV, which results in  $\varepsilon(0/-)$  close to the VBM.

Hartree-Fock-based hvbrid functional calculations, we previously found that even in a perfect supercell, adding or removing an electron from the system will give rise to mid-gap electronic states without creating any atomic defect [67]. By cutting the long-range part of exchange interaction, the HSE functional can mitigate this problem. To confirm these deep donor defects, we employed a 320-atom supercell to calculate the  $V_{Zr}$ ,  $S_i$ , and  $S_{Ba}$  defects and found that the  $\varepsilon(0/+)$  level are 1.28, 1.34 and 1.40 eV, respectively, below the CBM, which differ from the results using the 160-atom supercell by 0.07, 0.01 and 0.01 eV, respectively, suggesting the accuracy using the 160-atom supercell.

Finally, we discuss the Ba<sub>Zr</sub> defect. Our calculation shows that it is an amphoteric defect with its neutral charge state being unstable regardless of the position of the Fermi level. While being a deep acceptor, Bazr is also a shallow donor. Compared with the case of  $V_{2r}$ , the presence of an extra Ba atom hinders the formation a S-trimer. Without forming the S-trimer, its neutral state exhibits unpaired electrons, as shown in Figure 6, with magnetic moment of 2  $\mu_B$ . As mentioned above, the  $V_{\rm Zr}$ defect without forming the S-trimer is already a relatively deep acceptor. Here, the acceptor level of Bazr is even deeper (0.46 eV above the VBM) partly because of the presence of Ba cation which could stabilizes the captured electron by coulomb interaction. However, if being positively charged, a S-dimer will form with a S-S distance of 2.06 Å giving rise to a relatively shallow donor level of 0.14 eV below the CBM. Again, the flexibility of S anions forming the S-clusters significantly influences the behavior of Bazr similar to the other deep-level defects discussed above. However, different from the deep defect discussed above, its contains unoccupied state significant contribution from the S 3p orbitals, which are hybridized with the Zr 4d states (see Figure S3 in Supporting Information). For the other deep defects, their lowest unoccupied states are pure Zr 4d orbitals (see Figure S4 in Supporting Information). The highest occupied state of the Bazr defect is a localized state mainly contributed by S 3 p orbitals.

**Defect formation energy.** We next calculated the defect formation energies of the intrinsic defects using HSE functional. We first determined the allowed region for the chemical potentials that enables the formation of the primary phase of  $BaZrS_3$  while avoiding possible secondary phases. We considered the two secondary phases, BaS in the rock-salt structure and  $ZrS_2$  in the T structure. The calculated enthalpy of formation of T structure. The calculated enthalpy of formation of T and T structure elements are T and T structure.

The elements were calculated using the *bcc* Ba, *hcp* Zr and S in the  $\alpha$ -phase. The formation energy of BaZrS<sub>3</sub> with respect to BaS and ZrS<sub>2</sub> is thus -0.33 eV per formula unit. As shown in Figure 7a, the allowed region for the chemical potentials is bounded by the D, E, F, and G points. The values of the chemical potentials at these points are listed in Figure 7a.

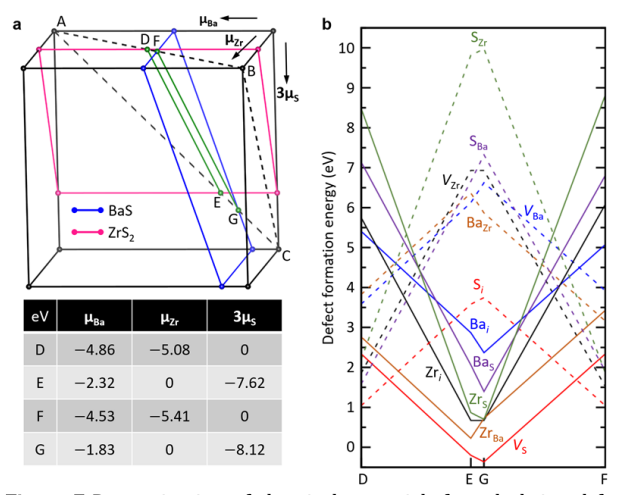


**Figure 7** Determination of chemical potentials for calculating defect formation energies in BaZrS<sub>3</sub>. (a) The triangle ABC is determined by  $\mu_{\rm Ba} + \mu_{\rm Zr} + 3\,\mu_{\rm S} = \Delta H({\rm BaZrS_3}) = -9.94$  eV. The allowed region DEGF is determined by the relations  $\mu_{\rm Ba} + \mu_{\rm S} \leq \Delta H({\rm BaS}) = -4.53$  eV and  $\mu_{\rm Zr} + 2\,\mu_{\rm S} \leq \Delta H({\rm ZrS_2}) = -5.08$  eV. The lower panel of (a) shows the chemical potentials of ( $\mu_{\rm Ba}$ ,  $\mu_{\rm Zr}$ ,  $3\,\mu_{\rm S}$ ) at the D, E, F and G points. (b) Defect formation energies of 12 intrinsic defects in BaZrS<sub>3</sub> at the D, E, G and F points calculated by the HSE function in the neutral state.

The calculated defect formation energies in the neutral charge state are shown in Figure 7b. Interestingly, the deep level defects, i.e., Bazr, Vzr, Si, SBa and Szr, all have rather high formation energies as long as the chemical potential moves slightly away from the D and F points, which corresponds to S-rich conditions. The low energy defects with formation energy less than 1 eV are Vs, Zri, ZrBa and Zrs, which are all shallow donors. The only shallow acceptor  $V_{Ba}$  has a formation energy of at least 3.6 eV. Therefore, we conclude that BaZrS<sub>3</sub> cannot be intrinsically p-type. This is different from previous conclusion using PBE+U calculation, which suggests that the material can be grown p-type if the growth condition is controlled at S-rich condition [31]. Figure 7b shows that  $V_S$  is the dominant defect that governs the conduction type of the material, which is consistent with our recent experiment on BaZrS<sub>3</sub> thin films [37]. Our results also suggest that Zr as a transition metal element is reactive enough to form sufficient bonding with neighboring S atoms to lower its formation energy when inserted into the lattice as an interstitial. In particular, the ZrBa antisite defect is the second lowest in formation energy over a large region of chemical potentials, which also happens to be a shallow donor. Under S-rich condition, S<sub>i</sub> defect may form if the synthesis temperature is sufficiently high and the annealing process is not sufficiently long.

#### CONCLUSIONS

We carried out a comparative study on the intrinsic defects of chalcogenide perovskite BaZrS3 using different DFT functionals and considering both the Hubbard *U* effect and the Hartree-Fock exchange. We show that tunning band gap towards the experimental value requires unphysically large U value, which in turn results in over-localization of the electronic states and deep defect levels. Using U and J values of 1.37 and 0.24 eV, respectively, determined from first-principles calculation, we found that the intrinsic defects of BaZrS<sub>3</sub> are all shallow-level defects, similar to the results obtained from the PBEsol functional, where  $\ensuremath{\emph{V}}_{Ba}$  and  $Ba_{Zr}$  are shallow acceptors,  $V_s$ ,  $Ba_i$ ,  $Zr_i$ ,  $Zr_{Ba}$ ,  $Ba_s$  and  $Zr_s$  are shallow donors, and  $V_{Zr}$ ,  $S_i$ ,  $S_{Ba}$  and  $S_{Zr}$  behave as self-passivated defects (*i.e.*, without "dangling bond" mid-gap states) in the neutral charge state. The self-passivation behavior is achieved by the formation of small S clusters and is highly desirable for a semiconductor being defect tolerant. In HSE calculations,  $V_{\rm Zr}$ , S<sub>i</sub>, S<sub>Ba</sub> and S<sub>Zr</sub> show deep donor levels emerging from the VBM suggesting that the self-passivation is not thorough. Nevertheless, all the deep-level defects from HSE, including Bazr, show high formation energies, especially when the experimental condition is not extremely S-rich. With these results, we conclude that BaZrS<sub>3</sub> is sufficiently defect tolerant, which is desirable for photovoltaic and optoelectronic applications.

## Received xxx 2015; accepted xxx 2015; Published online xxx 2015

- 1 Kojima A, Teshima K, Shirai Y, Miyasaka T. Organometal halide perovskites as visible-light sensitizers for photovoltaic cells. J Am Chem Soc, 2009, 131: 6050-6051
- 2 Lee M M, Teuscher J, Miyasaka T, *et al.* Efficient hybrid solar cells based on meso-superstructured organometal halide perovskites. Science, 2012, 338: 643-647
- perovskites. Science, 2012, 338: 643-647

  3 Burschka J, Pellet N, Moon S J, et al. Sequential deposition as a route to high-performance perovskite-sensitized solar cells. Nature, 2013, 499: 316-319
- 4 Liu M, Johnston M B, Snaith H J. Efficient planar heterojunction perovskite solar cells by vapour deposition. Nature, 2013, 501: 395-398
- 5 Green M A, Ho-Baillie A, Snaith H J. The emergence of perovskite solar cells. Nat Photonics, 2014, 8: 506-514
- 6 Jeon N J, Noh J H, Yang W S, et al. Compositional engineering of perovskite materials for high-performance solar cells. Nature, 2015, 517: 476-480
- 7 Saliba M, Matsui T, Domanski K, *et al.* Incorporation of rubidium cations into perovskite solar cells improves photovoltaic performance. Science, 2016, 354: 206-209
- 8 McMeekin D P, Sadoughi G, Rehman W, *et al.* A mixed-cation lead mixed-halide perovskite absorber for tandem solar cells. Science, 2016, 351: 151-155
- 9 Fang Y, Dong Q, Shao Y, *et al.* Highly narrowband perovskite single-crystal photodetectors enabled by surface-charge recombination. Nat Photonics, 2015, 9: 679-688

**ARTICLES** 

- 10 Büchele P, Richter M, Tedde S F, et al. X-ray imaging with scintillator-sensitized hybrid organic photodetectors. Nat Photonics, 2015, 9: 843-848
- 11 Tan Z, Y Wu, Hong H, et al. Two-dimensional (C<sub>4</sub>H<sub>9</sub>NH<sub>3</sub>)<sub>2</sub>PbBr<sub>4</sub> perovskite crystals for high-performance photodetector. J Am Chem Soc, 2016, 138: 16612-16615
- 12 Kim Y C, Kim K H, Son D Y, D. et al. Printable organometallic perovskite enables large-area, low-dose X-ray imaging. Nature, 2017, 550: 87-91
- 13 Chen Q, Wu J, Ou X, et al. All-inorganic perovskite nanocrystal scintillators. Nature, 2018, 561: 88-93
- 14 Tan Z K, Moghaddam R S, Lai M L, et al. Bright light-emitting diodes based on organometal halide perovskite. Nat Nanotechnol, 2014, 9: 687-692
- 15 Stranks S D, Snaith H J. Metal-halide perovskites for photovoltaic and light-emitting devices. Nat Nanotechnol, 2015,
- 16 Cho H, Jeong S -H, Park M -H, et al. Overcoming the electroluminescence efficiency limitations of perovskite light-emitting diodes. Science, 2015, 350, 1222-1225
- 17 Swarnkar A, Marshall A R, Sanehira E M, et al. Quantum dot-induced phase stabilization of α-CsPbI<sub>3</sub> perovskite for high-efficiency photovoltaics. Science, 2016, 354: 92-95
- 18 Zhang L, Yang X, Jiang Q, et al. Ultra-bright and highly efficient inorganic based perovskite light-emitting diodes. Nat Commun, 2017, 8: 1-8
- 19 Xiao Z, Kerner R A, Zhao L, et al. Efficient perovskite light-emitting diodes featuring nanometre-sized crystallites.
- Nat Photonics, 2017, 11: 108-115

  20 Lin K, Xing J, Quan L N, *et al.* Perovskite light-emitting diodes with external quantum efficiency exceeding 20 per cent. Nature, 2018, 562: 245-248
- 21 You Y -M, Liao W -Q, Zhao D, *et al.* An organic-inorganic perovskite ferroelectric with large piezoelectric response. Science, 2017, 357: 306-309
- 22 Zhang S, Li F, Jiang X, et al. Advantages and challenges of relaxor-PbTiO<sub>3</sub> ferroelectric crystals for electroacoustic transducers - A review. Prog Mater Sci, 2015, 68: 1-66
- 23 Amat A, Mosconi E, Ronca E, et al. Cation-induced band-gap tuning in organohalide perovskites: Interplay of spin-orbit coupling and octahedra tilting. Nano Lett, 2014, 14: 3608-3616
- 24 McGehee M D. Fast-track solar cells. Nature, 2013, 501:
- 25 Grätzel M. The light and shade of perovskite solar cells. Nat Mater, 2014, 13: 838-842
- 26 Hahnand H, Mutschke U. Untersuchungen über ternäre Chalkogenide. XI. Versuche zur darstellung von thioperowskiten. Z Anorg Allg Chem, 1957, 288: 269-278
  27 Ishii M, Saekiand M, Sekita M. Vibrational spectra of barium-zirconium sulfides. Mater Res Bull, 1993, 28: 493-500
- 28 Bennett J W, Grinbergand I, Rappe A M. Effect of substituting of S for O: The sulfide perovskite the sulfide perovskite BaZrS<sub>3</sub> investigated with density functional theory. Phys Rev B, 2009,
- 29 Brehm J A, Bennett J W, Schoenberg M R, et al. The structural diversity of ABS3 compounds with do electronic configuration for the B -cation. J Chem Phys, 2014, 140: 0-8
- 30 Sun Y Y, Agiorgousis M L, Zhang P, Zhang S. Chalcogenide perovskites for photovoltaics, Nano Lett, 2015, 15: 581-585
- 31 Meng W, Saparov B, Hong F, et al. Alloying and defect control within calcogenide perovskites for optimized photovoltaic application. Chem Mater, 2016, 28: 821-829
- 32 Ju M G, Dai J, Ma L, Zeng X C. Perovskite chalcogenides with optimal bandgap and desired optical absorption for photovoltaic devices. Adv Energy Mater, 2017, 7: 2-8
- 33 Perera S, Hui H, Zhao C, et al. Chalcogenide perovskites an emerging class of ionic semiconductors. Nano Energy, 2016, 22:
- 34 Niu S, Huyan H, Liu Y, et al. Bandgap control via structural and chemical tuning of transition metal perovskite chalcogenides.
- Adv Mater, 2017, 29: 1604733 35 Gross N, Sun Y Y, Perera S, *et al.* Stability and band-gap tuning of the chalcogenide perovskite BaZrS3 in raman and optical

- investigations at high pressures. Phys Rev Appl, 2017, 8: 1-10
- 36 Wei X, Hui H, Perera S, *et al.* Ti-alloying of BaZrS<sub>3</sub> chalcogenide perovskite for photovoltaics. ACS Omega, 2020, 5: . 18579-18583
- 37 Wei X, Hui H, Zhao C, et al, Realization of BaZrS<sub>3</sub> chalcogenide perovskite thin films for optoelectronics. Nano Energy, 2020,
- 38 Comparotto C, Davydova A, Ericson T, et al. Chalcogenide perovskite BaZrS<sub>3</sub>: Thin film growth by sputtering and rapid thermal processing. ACS Appl Energy Mater, 2020, 3: 2762-2770
- 39 Gupta T, Ghoshal D, Yoshimura A, et al. An environmentally stable and lead-free chalcogenide perovskite. Adv Funct Mater, 2020, 30: 2001387
- 40 Hanzawa K, Iimura S, Hiramatsu H, Hosono H. Material design of green-light-emitting semiconductors: Perovskite-type sulfide SrHfS<sub>3</sub>. J Am Chem Soc, 2019, 141: 5343-5349
- 41 Zhang H, Ming C, Yang K, et al. Chalcogenide perovskite YScS<sub>3</sub> as a potential p-type transparent conducting material. Chinese Phys Lett, 2020, 37: 097201
- 42 Yin W -J, Shi T, Yan Y. Unusual defect physics in CH<sub>3</sub>NH<sub>3</sub>Pb<sub>3</sub> perovskite solar cell absorber. Appl Phys Lett, 2014, 104:
- 43 Yin W, Shi T, Y. Yan. Unique properties of halide perovskites as possible origins of the superior solar cell performance. Adv Mater, 2014, 26: 4653-4658
- 44 Agiorgousis M L, Sun Y Y, Zeng H, Zhang S. Strong covalency-induced recombination centers in perovskite solar cell material CH3NH3PbI3. J Am Chem Soc, 136:14570-14575
- 45 Brandt R E, Stevanović V, Ginley D S, Buonassisi T. Identifying defect-tolerant semiconductors with high minority-carrier lifetimes: Beyond hybrid lead halide perovskites. MRS Commun, 2015, 5: 265-275
- 46 Meggiolaro D, Motti S G, Mosconi E, *et al.* Iodine chemistry determines the defect tolerance of lead-halide perovskites. Energy Environ Sci, 2018, 11: 702-713
- 47 Kurchin R C, Gorai P, Buonassisi T, Stevanović V. Structural and chemical features giving rise to defect tolerance of binary semiconductors. Chem Mater, 2018, 30: 5583-5592
- 48 Park J S, Kim S, Xie Z, Walsh A. Point defect engineering in thin-film solar cells. Nat Rev Mater, 2018, 3: 194-210
- 49 Kang J, Wang L. High defect tolerance in lead halide perovskite CsPbBr<sub>3</sub>. J Phys Chem Lett, 2017, 8: 489-493
- 50 Kresse G, Furthmüller J. Efficiency of ab-initio total energy calculations for metals and semiconductors using a plane-wave basis set. Comp Mater Sci, 1996, 6:15-50
- 51 Blöchl P E. Projector augmented-wave method. Phys Rev B, 1994, 50: 17953-17979
- 52 Kresse G, Joubert D. From ultrasoft pseudopotentials to the projector augmented-wave method. Phys Rev B, 1999, 59: 1758-1775
- 53 Perdew J P, Ruzsinszky A, Csonka G I, et al. Restoring the Density-gradient expansion for exchange in solids and surfaces. Phys Rev Lett, 2008, 100: 136406
- 54 Dudarev S L, Botton G A, Savrasov S Y, et al. Electron-energy-loss spectra and the structural stability of nickel oxide: An LSDA+U study. Phys Rev B, 1998, 57: 1505-1509
- 55 Heyd J, Scuseria G E, Ernzerhof M. Hybrid functionals based on a screened Coulomb potential. J Chem Phys, 2003, 118, 8207-8215
- 56 Lelieveld R, IJdo D J W. Sulphides with the  $GdFeO_3$  structure. Acta Crystallogr, 1980, 36: 2223-2226
- 57 Zhang S, Northrup J. Chemical potential dependence of defect formation energies in GaAs: Application to Ga self-diffusion. Phys Rev Lett, 1991, 67: 2339-2342
- 58 Freysoldt C, Grabowski B, Hickel T, et al. First-principles calculations for point defects in solids. Rev Mod Phys, 2014, 86:
- 59 Miyake T, Aryasetiawan F, Imada M. Ab initio procedure for constructing effective models of correlated materials with entangled band structure. Phys Rev B, 2009, 80: 155134

60 Shih B -C, Abtew T A, Yuan X, *et al.* Screened Coulomb interactions of localized electrons in transition metals and transition-metal oxides. Phys Rev B, 2012, 86: 165124

- 61 Shih B -C, Zhang Y, Zhang W, Zhang P. Screened Coulomb interaction of localized electrons in solids from first principles. Phys Rev B, 2012, 85: 045132
- 62 Liu C, Yang Y, Xia X, et al. Soft template-controlled growth of high-quality CsPbI<sub>3</sub> films for efficient and stable solar cells. Adv Energy Mater, 2020, 10: 1-10
- 63 Mostofi A A, Yates J R, Lee Y -S, *et al.* wannier90: A tool for obtaining maximally-localised Wannier functions, Comput Phys Commun, 2008, 178: 685-699
- 64 Deslippe J, Samsonidze G, Strubbe D A, et al. BerkeleyGW: A massively parallel computer package for the calculation of the quasiparticle and optical properties of materials and nanostructures. Comput Phys Commun, 2012, 183: 1269-1289
- 65 Leslie M, Gillan N J. The energy and elastic dipole tensor of defects in ionic crystals calculated by the supercell method. J Phys C Solid State Phys, 1985, 18: 973-982
- 66 Heyd J, Peralta J E, Šcuseria G E, Martin R L. Energy band gaps and lattice parameters evaluated with the Heyd-Scuseria-Ernzerhof screened hybrid functional. J Chem Phys, 2005, 123: 174101
- 67 Bang J, Sun Y Y, Abtew T A, *et al.* Difficulty in predicting shallow defects with hybrid functionals: Implication of the long-range exchange interaction. Phys Rev B, 2013, 88: 035134 (2013).

Acknowledgements This work was financially supported by National Natural Science Foundation of China (11774365), Natural Science Foundation of Shanghai (19ZR1421800), Shanghai International Cooperation Project (20520760900), Opening Project and Science Foundation for Youth Scholar of State Key Laboratory of High Performance Ceramics and Superfine Microstructures (SKL201804, SKL201803SIC). H.Z. thanks the support by US NSF (CBET-1510121) and DOE (DEEE0007364). S.Z. thanks the support by US NSF (CBET-1510948). P.Z. thanks the support by US NSF (DMR-1506669). W.G. thanks the support by the Fundamental Research Funds for the Central Universities (DUT21RC(3)033) and the computational resources provided by NERSC of the US DOE (DEACO2-05CH11231), the Texas Advanced Computing Center (TACC) and Shanghai Supercomputer Center.

**Author contributions** Sun YY initiated and coordinated the research. Wu X, Chai J and Ming C conducted the defect calculations. Gao W and Zhang P conducted the RPA calculations. Chen M, Zeng H and Zhang S participated in the analysis of the results. Sun YY, Wu X, Gao W, Ming C, Zeng H, Zhang P and Zhang S wrote the paper.

 $\begin{tabular}{ll} \textbf{Conflict of interest} The authors declare that they have no conflict of interest. \end{tabular}$ 

**Supplementary information** Supporting data are available in the online version of the paper.



**Xiaowei Wu** received her BSc degree from the School of Physics and Electronic Information Engineering, Neijiang Normal University in 2016, and her Master degree from the School of Resources, Environment and Materials, Guangxi University in 2020. She joined the State Key Laboratory of High Performance Ceramics and

Superfine Microstructure, Shanghai Institute of Ceramics, Chinese Academy of Sciences in 2020 as a Research Assistant. Her current research focuses on the defect properties in energy materials using first-principles calculations.



**Weiwei Gao** is currently an associate professor at School of Physics, Dalian University of Technology. He received his PhD degree from Department of Physics, The State University of New York at Buffalo and did postdoctoral research in Oden Institute for Computational Engineering and Sciences, University of Texas at Austin. His research interests focus on developing new methods for efficient excited-states calculations and applying computational approach on studying novel materials.



**Chen Ming** received his Ph.D. from Fudan University in 2012. He joined the State Key Laboratory of High Performance Ceramics and Superfine Microstructure, Shanghai Institute of Ceramics, Chinese Academy of Sciences in 2014 as a postdoc and then as a research associate. His research interests are theoretical explorations of novel materials for optoelectronics and energy applications.



**Yi-Yang Sun** received his PhD degree from National University of Singapore (NUS) in 2004. He has worked as postdoc at NUS, National Renewable Energy Laboratory, and Rensselaer Polytechnic Institute (RPI). In 2010, he was appointed research assistant professor and later research scientist at RPI. In 2017, he assumed a professor position at Shanghai Institute of Ceramics, Chinese Academy of Sciences. His research focuses on the study of energy-related materials using the first-principles computations.

### 硫族钙钛矿光伏材料BaZrS3的缺陷容忍性

吴晓维 $^{1,\dagger}$ ,高威帷 $^{2,3,\dagger}$ ,柴骏 $^{1}$ ,明辰 $^{1,*}$ ,陈苗根 $^{4}$ ,曾浩 $^{5}$ ,张培鸿 $^{5}$ ,张绝百 $^{6}$ ,孙宜阳 $^{1,*}$ 

摘要 硫族钙钛矿具有比氧化物钙钛矿更低的带隙以及比卤化物钙钛矿更高的稳定性,有望应用于光伏和光电领域。在这类应用中,理想的材料往往需要避免作为复合中心的深能级缺陷的存在,即缺陷容忍性。本文采用密度泛函理论(DFT),研究一种典型硫族钙钛矿材料BaZrS3的本征缺陷。我们比较了Hubbard-*U*和杂化泛函这两种广泛用于解决DFT中半局域泛函带隙问题的方法。研究发现,通过调整*U*值获得与实验一致的带隙,并将该*U*值用于缺陷计算,可能会导致缺陷态过度局域化。而杂化泛函计算则可以准确得到BaZrS3的带隙。我们观察到采用这两种计算方法均会形成小的S原子团簇,的带隙。我们观察到严重、中深能级的产生。尽管在杂化泛函计算中观察到一些能级相对较深的缺陷,但是在热平衡条件下制备的材料中,如于过高的形成能,这些缺陷的作用可以被忽略。因此,BaZrS3具有足够的缺陷容忍性,有望应用于光伏和光电领域。